PERFORMANCE ASSESSMENT OF THE MULTIBEAM RADAR SENSOR BIRALES FOR SPACE SURVEILLANCE AND TRACKING

Pierluigi Di Lizia[(1)], Mauro Massari[(1)], Matteo Losacco[(1)], Germano Bianchi[(2)], Andrea Mattana[(2)], Giuseppe Pupillo[(2)], Claudio Bortolotti[(2)], Mauro Roma[(2)], Alessandro Morselli[(3)], Roberto Armellin[(4)], Alessio Magro[(5)], Denis Cutajar[(5)], Claudio Portelli[(6)], Marco Reali[(7)]

[(1)] Department of Aerospace Science and Technology, Politecnico di Milano, Via G. La Masa 34, 20156 Milano, Italy, {pierluigi.dilizia, mauro.massari, matteo.losacco}@polimi.it

[(2)] Istituto Nazionale di Astrofisica - Istituto di Radioastronomia, Via P. Gobetti 101, 40129 Bologna, Italy, {g.bianchi, a.mattana, g.pupillo, c.bortolotti, m.roma}@ira.inaf.it

[(3)] European Space Agency (ESA/ESOC), Robert-Bosch-Str. 5, 64293 Darmstadt, Germany, alessandro.morselli@esa.int

[(4)] Surrey Space Center, University of Surrey, GU2 7XH Guilford, United Kingdom, r.armellin@surrey.ac.uk

[(5)] University of Malta, Msida MSD 2080, Malta, {alessio.magro, denis.cutajar}@um.edu.mt

[(6)] Italian Space Agency, Via del Politecnico snc, 00133 Roma, Italia, claudio.portelli@asi.it

[(7)] Italian Air Staff – ITAF, Viale dell'Università 4, 00185 Rome, Italy, marco.reali@aeronautica.difesa.it

ABSTRACT

Near-Earth space has become progressively more crowded in active satellites, inactive spacecraft and debris. Consequently, an international effort is currently being devoted to improving the performance of the network of optical and radar sensors for space objects monitoring. Within this framework, the use of the novel bistatic radar sensor BIRALES is investigated in this work, which makes use of a multibeam receiver. The tailored orbit determination algorithm is described, which receives as input the data processed by the acquisition system, that digitally assembles measured radar echoes. The performance**s** of the orbit determination process are assessed on a set of numerical simulations carried out on the NORAD catalogue, using a dedicated simulator of the sensor.

1 INTRODUCTION

The number of manmade objects orbiting the Earth has dramatically increased during the last decades, posing a serious risk for space based activities. Most of the objects currently orbiting the Earth are classified as space debris, that include inactive satellites, discarded launch stages, and fragments originated from satellite breakups and collisions. Several counter measures have been adopted with the aim of reducing mission related risks and casualties and to control the number of objects in orbit. Mitigation guidelines have been published by various organisations such as the Inter-Agency Space Debris Coordination (IADC) committee and the United Nations (UN). The general aim of space debris mitigation is to reduce the growth of space debris by ensuring that space systems are designed, operated, and disposed of in a manner that prevents them from generating debris throughout their orbital lifetime. In parallel specific space programs were started to build the expertise required to manage the challenges posed by the space traffic control problem. Collision risk assessment is performed daily by satellite operators and conjunction summary messages are provided to satellite operators by the United States Strategic Command (USSTRATCOM) to support decisions on the execution of collision avoidance manoeuvres [1]. In addition, re-entry predictions of objects are regularly produced to estimate on ground risks [2]. Both collision risk assessment and re-entry predictions rely on the accurate estimation of the state of the orbiting objects and of their evolution, which is derived from the tracking of the space objects using dedicated optical, radar, and laser sensors.

Survey and tracking of objects in Earth orbit is one of the main areas where the European Space Surveillance and Tracking (SST) Support Framework and the ESA Space Situational Awareness (SSA) programmes are active [3, 4]. The objective of such initiatives is to support the European utilization of and access to space through the provision of information and data on the space environment. To meet this requirement, the implementation of a European network of sensors for surveillance and tracking of objects in Earth's orbit is mandatory. Within this framework, the Italian Northern Cross radio telescope array has been upgraded to serve the European SST Framework as a component of the Italian contribution to the European network for SST in the frame of the BIstatic RAdar for LEo Survey (BIRALES) sensor [5].

Proc. 7th European Conference on Space Debris, Darmstadt, Germany, 18–21 April 2017, published by the ESA Space Debris Office
Ed. T. Flohrer & F. Schmitz, (http://spacedebris2017.sdo.esoc.esa.int, June 2017)

BIRALES uses part of the Northern Cross radiotelescope located in Medicina (Bologna, Italy) as the receiver (see Fig. 1). Part of the radiotelescope has been refurbished and a digital backend has been implemented to allow beamforming of 32 beams distributed across the receiver field of view (FoV). When an object transits inside the antenna FoV, the beams are illuminated by the reflected radio wave. Consequently, besides the classical range and Doppler shift measurements, the beam illumination sequence provides an estimate of the transit direction of the scattering object and of the associated right ascension and declination profiles. The data received from BIRALES are provided as input to a tailored orbit determination (OD) algorithm, which is aimed at computing an estimate of the orbital parameters of the observed object.

Figure 1. A view of the Medicina Radioastronomical Station. In the foreground, the Northern Cross array

A numerical simulator of BIRALES has been developed to assess its performance through dedicated simulations. Given a catalogue of space objects, the simulator identifies the passages of all the objects in the sensor FoV during a simulated observation campaign. Then, the simulated measurements are generated for each passage and are provided as input to the OD module, along with the required transmitter and receiver information. The simulator is designed so that different kind of transmitter and beams geometry can be easily defined by the user. This enables an effective analysis of the sensitivity of the sensor to its configuration, which is instrumental to optimizing its performances.

This paper illustrates the results achieved with the numerical simulations campaign. The performance of the sensor is assessed using different multibeam configurations, sensor pointing strategies, and first guess generation approaches. For each configuration, the simulation is run on a catalogue of Two Line Elements (TLEs) downloaded from Space-Track (www.space-track.org). In addition, both the case of known objects (first guess for the OD process generated from the TLE) and unknown objects (first guess for the OD process generated from the measurements) are investigated.

2 BISTATIC RADAR FOR LEO SURVEY (BIRALES) SENSOR

Ground-based radars provide a powerful tool for the characterization of the orbital debris environment. Radars can in fact irradiate at any time a satellite or space debris in Earth orbit with a microwave beam. The scattered wave can be detected by a receiver, which may be the same transmitting antenna (monostatic radar) or a different one located at a distance of up to several hundreds of kilometers away (bistatic radar).

The proposed sensor uses a bistatic configuration. The "Flight Termination System" (FTS) of the Italian Joint Test Range of Salto di Quirra (PISQ) in Sardinia is used as transmitter (Fig.2), and the Northern Cross radiotelescope of the radioastronomy station of Medicina (BO) as receiver.

The FTS is a powerful transmitter, owned by the Italian Air Force, presently used for safety purposes during the system trials at PISQ. The FTS consists in a power amplifier able to supply an average and levelled power of 4 kW in the bandwidth 400-455 MHz coupled with an Omnidirectional Antenna and wide beam directional antenna. The transmitter is usually used in CW mode, anyway the equipment is able to receive in input a modulated signal. Clearly the use in CW mode does not enable the bi-static sensor to detect the range of the object, whereas using a dedicated, synchronized waveform and applying the right modulation signal enables the ranging capability.

Figure 2. The "Flight Termination System" (FTS) transmitter

The Northern Cross represents the largest UHF-capable antenna in Northern hemisphere. It is composed of two perpendicular arms: the E/W (East-West) arm is 564 m long and consists of a single cylindrical antenna with a width of 35 m, whereas the N/S (North-South) arm is made of 64 parallel antennas with a length of 23.5 m and a width of 8 m each. The collecting area reaches 27,000 m^2 and, due to the large numbers of receivers which could be installed on the focal lines, the FoV can be populated with many independent beams. When an object transits inside the antenna FoV, the beams are illuminated by the reflected radio wave. By looking at the beam illumination sequence, it is thus possible to estimate the ground track of the transiting object, with a higher level of detail with respect to a single-beam system (Fig. 3). The acquired data is processed by means of a data acquisition system, which digitally assembles measured radar echoes using a Fast Fourier Transform (FFT) in spatial domain in order to calculate the signal present in each beam. Doppler shift, the illumination time, and measured power intensity associated to each beam are thus available.

The same bistatic architecture could be used to perform ranging, provided that the transmission signal is modulated with pulse compression waveforms, transmitter and receiver are synchronized and the data processing chain contains a ranging estimation block. The bistatic radar shall use a ranging waveform based on pulse compression technique. The bandwidth needed to obtain the requested ranging performances is largely inside the transmitter and receiver characteristics. A frequency modulated signal shall be generated in the expander unit, up converted and sent to the transmitter. A high duty cycle transmission pattern (very long pulses at high repetition rate) shall supply an average power sufficient to guarantee detection and range extraction at the requested range. The transmitted waveform and its matched filter in the receiving branch shall be designed to obtain a good sidelobes level taking into consideration the Doppler shift due to the target motion. Pulse compression shall be performed digitally in the receiver part and the resulting ambiguous video shall be sent to range extraction algorithms. Range ambiguity shall be solved taking into consideration the geometry and a rough target range estimate. The system can quickly switch from the multi-beaming observation mode (performed in continuous wave) to ranging mode: during the transit of an object both types of measurement can be thus acquired.

This paper focuses on a possible future configuration of the sensor. It uses a transmitter upgraded to generate 10 kW with a wide parabolic antenna (7 m of diameter), capable to track the receiver multibeam pattern and to provide ranging information. As a receiver, only a small part of the Northern Cross antenna, named BEST-2 [6] (Basic Element for Ska Training) is used (Fig. 4).

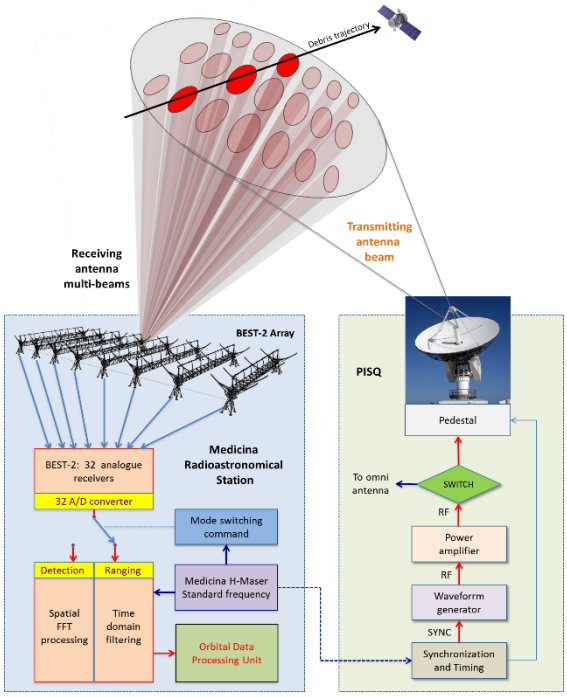

Figure 3. Schematic block and example of space debris trajectory detection using BIRALES

BEST-2 is an array composed of 8 cylindrical parabolic concentrators belonging to the N-S arm operating in a band of 14 MHz centered at 408 MHz. The total collective area is about 1,400 m^2. Each cylinder contains four receivers connected to 16 dipoles each (Fig. 5). The total array contains 32 receivers that enable the realization of a multibeam receiver antenna.

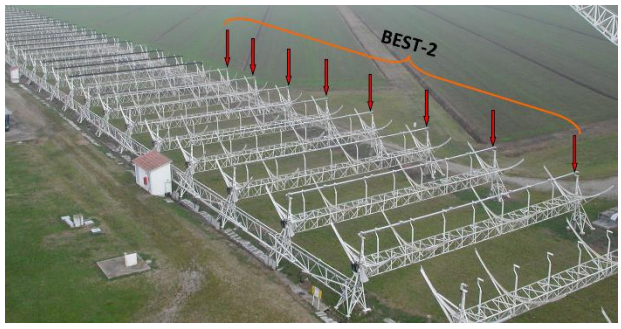

Figure 4. BEST-2 antennas

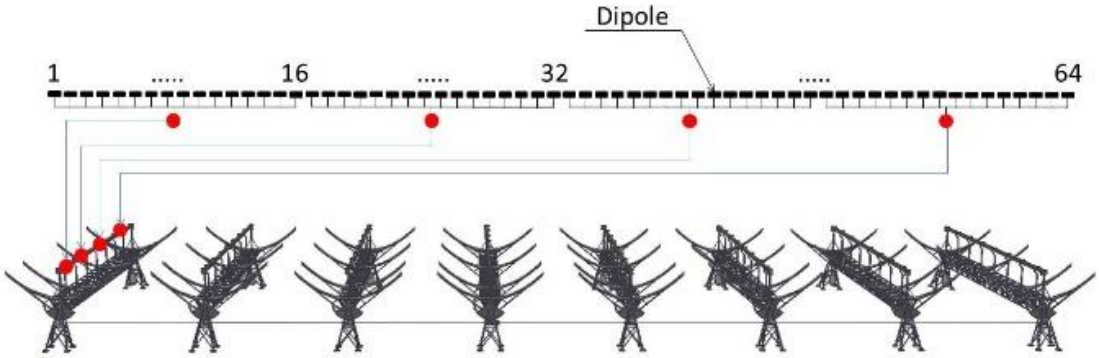

Figure 5. Single BEST-2 antenna architecture

The signals scattered from the object are then processed to estimate the orbital parameters. Tailored OD algorithms were developed so that, using both the ranging and the beam illumination sequence, the orbital parameters of the transiting object can be estimated. By combining this information with the knowledge of the beam distribution and antenna pointing, it is possible to refine the orbital parameters of known objects or to perform a preliminary OD (see Section 4).

3 BIRALES SIMULATOR

A simulator of the bistatic radar configuration described above was developed to support analysis and to estimate the system performance. It has also the capability of generating data resembling those that could be measured in reality. The simulator is designed so that different kind of transmitter and multibeam geometry can be easily defined by the user. A scheme of the architecture of the simulator is reported in Fig. 6.

The simulator is made of the following main modules:

Passage identification: Given the catalogue of the space objects and the associated TLEs, the passage identification module propagates the motion of the objects using the Simplified General Perturbations #4 (SGP4) model and identifies, in a given time interval, all the passages on the BIRALES sensor. In addition, the module provides the main parameters characterizing the passage, such as the epoch and the required pointings.

Measurements generation: For all the passages identified by the passage identification module, the simulator first derives the state of the object at the reference epoch of its TLE. Then, it propagates the motion of the object through its passage on BIRALES using the high-fidelity propagator AIDA (Accurate Integrator for Debris Analysis), which includes the gravitational model EGM2008 up to order 10, the atmospheric drag with the atmosphere model NRLMSISE-00, third body perturbations, and solar radiation pressure with a dual-cone model for Earth shadow. The resulting position and velocity profiles are used to generate the simulated measurements.

The computation of the simulated measurements is described hereafter. A sketch of the geometric configuration of a bistatic radar system is given in Fig. 7. A plane that contains the two relative distance vectors from the transmitter (Tx) and the receiver (Rx), ρ_{Tx} and ρ_{Rx} respectively, and the baseline L can be defined. This plane is usually indicated as *bistatic plane* and it allows for easy computations of all range relationships.

Given the trajectory of the object, ρ_{Tx} and ρ_{Rx} are directly computed using the positions of the two antennas. The time interval ΔT between the transmission of the pulse and the reception of the target echo is obtained from

$$\rho_{Tx} + \rho_{Rx} = c\Delta T \quad (1)$$

where c is the speed of light. The bistatic Doppler shift, when ignoring relativistic effects, is computed as

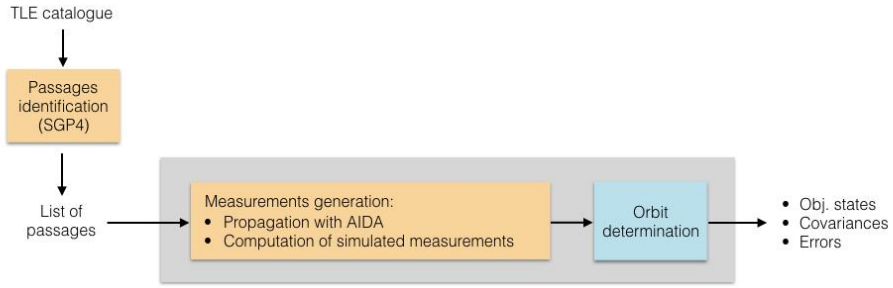

Figure 6. Architecture of the BIRALES simulator

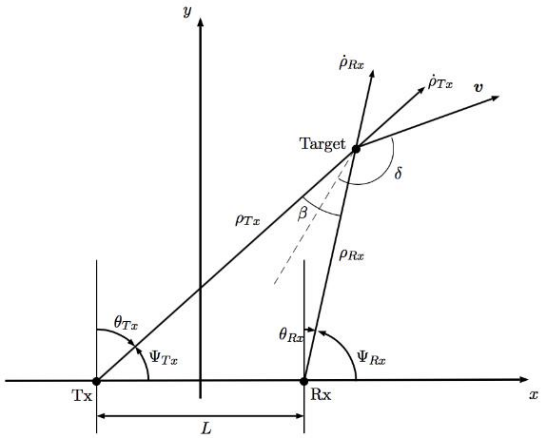

Figure 7. Geometry of the radar system on the bistatic plane

$$\Delta f = \frac{1}{\lambda}\left(\dot{\rho}_{Tx} + \dot{\rho}_{Rx}\right), \tag{2}$$

where λ is the wavelength of the transmitted signal and $\dot{\rho}_{Tx}$ and $\dot{\rho}_{Rx}$ are the projections of the target velocity onto the transmitter-to-target and receiver-to-target line of sight (LOS).

When both Tx and Rx are stationary, the Doppler shift becomes

$$\Delta f = \frac{2V}{\lambda}\cos\delta\cos\left(\frac{\beta}{2}\right). \tag{3}$$

Projecting the Earth-Centered Earth-Fixed (ECEF) velocity of the object v on the range vectors direction yields

$$\Delta f = \frac{1}{\lambda}\left(\boldsymbol{v}\cdot\hat{\boldsymbol{\rho}}_{Tx} + \boldsymbol{v}\cdot\hat{\boldsymbol{\rho}}_{Rx}\right). \tag{4}$$

For each beam of Rx is then possible to compute the received power using the bistatic radar equation

$$P_{Rx} = \frac{P_{Tx}\,G_{Tx}\,G_{Rx}\,\lambda^2\,\sigma_b}{(4\pi)^3\,\rho_{Tx}^2\rho_{Rx}^2}, \tag{5}$$

where P_{Tx} is the transmitter power, G_{Tx} and G_{Rx} are the antenna gains, and σ_b is the radar cross section. Where needed, the information on the satellite radar cross section are taken from a Space-Track catalogue downloaded on October 10, 2014.

At each time step the ranges ρ_{Tx} and ρ_{Rx} are obtained from orbit propagation and the antenna gains are updated using an elliptical model for the beam:

$$G_{dB} = G_{dB0} - 12\left(\left(\frac{\Delta\alpha}{BW_\alpha}\right)^2 + \left(\frac{\Delta\delta}{BW_\delta}\right)^2\right), \tag{6}$$

where $G_{dB} = 10\log_{10}G$, G_{dB0} is the reference gain of the antenna in decibel, $\Delta\alpha$ and $\Delta\delta$ are the angular deviations in right ascension and declination from beam center, and the beamwidths on the two axes of the ellipse are BW_α and BW_δ. Once the received power is obtained, the signal-to-noise ratio (SNR) is computed as

$$SNR = 10\log_{10}\frac{P_{Rx}}{k_B B_n T_0}, \tag{7}$$

in which k_B is the Boltzmann constant, B_n is the bandwidth of the receiver and T_0 is the noise temperature at the receiver.

Fig. 8 reports the illustration of a passage through the 32 beams distributed in the field of view of the sensor. The beams and the angles profiles are plotted in the $\Delta\alpha - \Delta\delta$ plane and colored according to their maximum value of SNR, normalized with respect to the maximum SNR among all beams. Non-illuminated beams are colored in black.

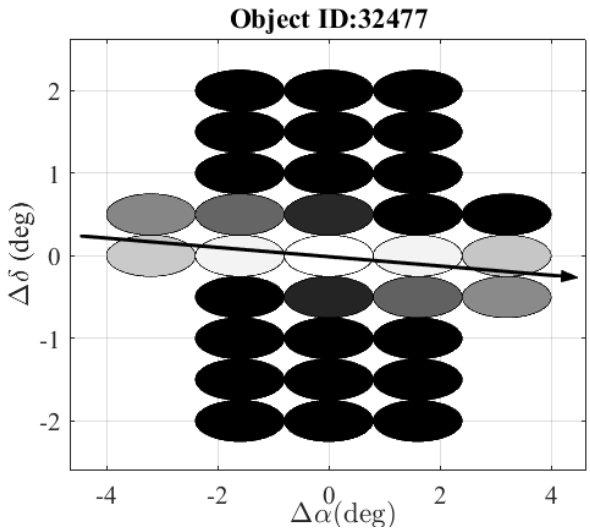

Figure 8. Passage inside the receiver FoV for object 32477

The resulting simulated measures are organized in a text file, reporting the measured ΔT, Δf, and SNR for each beam and for each time. The text file is the input to the OD algorithm.

4 ORBIT DETERMINATION ALGORITHM

This section illustrates the orbit determination algorithm. The cases of known and unknown object are studied, and the differences in the implementations are highlighted.

4.1 Known Objects

The case of known object refers to OD process performed for an object whose TLE is available to the user. In this situation, the orbit determination process is divided in two phases. The first phase consists in evaluating the topocentric deviation of the right ascension and declination, $\Delta\alpha$ and $\Delta\delta$, of the Resident Space Object (RSO) starting from the knowledge of SNR measurements. Then, the object position and velocity vectors are estimated using a least square fit.

The evaluation of $\Delta\alpha$ and $\Delta\delta$ is done assuming that the relative velocity of the debris with respect to the receiver is high enough to approximate the motion inside the FoV as a slightly curved line. Thus, the time history of the two parameters can be expressed as:

$$\begin{cases}\Delta\alpha = a_2 t^2 + a_1 t + a_0 \\ \Delta\delta = b_2 t^2 + b_1 t + b_0\end{cases} \quad (8)$$

where t is the time elapsed from the nominal epoch of observation of the object inside the FoV of the sensor. The estimation of the coefficients a_0, a_1, a_2, b_0, b_1 and b_2 is divided in two steps (referred to as S1 and S2 in the followings). In S1, the knowledge of the level of the measured SNR for each beam and the TLE of the observed object are combined. The procedure goes through the following steps:

- **S1-1.** For each illuminated beam, identify the time instant of maximum illumination, the related SNR, and the topocentric right ascension and declination of the center of the beam.
- **S1-2.** Perform a curve fit that minimizes the angular displacement from each beam centre at the time of the maximum received power. The selected weights are the normalized values of the SNR, using as a reference the maximum SNR among all beams.
- **S1-3.** Evaluate the topocentric $\Delta\alpha$ and $\Delta\delta$ time histories starting from the knowledge of the TLE of the observed object at a specific time epoch before the observation epoch and propagating the initial state vector by means of SGP4. This fictitious observation process provides the trace the object would have inside the receiver FoV if the dynamic was described by the approximated SGP4 model.
- **S1-4.** Rotate the solution obtained by the curve fit along the direction provided by the fictitious observation process.

The solution obtained with step S1 provides a rough estimation of the right ascension-declination profile inside the receiver FoV. In S2, the solution is refined with a least square aimed at minimizing the residuals between the measured SNR and their estimates, obtained with the $\Delta\alpha(t)$ and $\Delta\delta(t)$ guesses. The steps are the following:

- **S2-1.** Compute the azimuth and elevation of the target with respect to the receiver using the right ascension and declination of Eq.8 and the nominal pointing of each beam
- **S2-2.** Compute the look angle of the receiver using the azimuth and elevation of the target computed in the previous step and the azimuth and elevation of the transmitter
- **S2-3.** Compute the receiver and transmitter range
- **S2-4.** Compute the SNR for each beam
- **S2-5.** Evaluate the residuals with respect to the measured SNR's
- **S2-6.** Update the coefficients

The procedure provides at convergence the time history of the right ascension and declination inside the receiver FoV.

Fig.9 shows the results of the presented algorithms for the case of object 27421. Beams are coloured in grey scale according to the peak SNR measured during the passage (white corresponds to the largest measured SNR). The blue line represents the output of process S1, the approximated first guess, the red line represents the computed $\Delta\alpha(t)$ -$\Delta\delta(t)$, while the black line is the true trajectory of the object inside the receiver FoV. As can be seen, in this case the difference between the first two lines is almost negligible. This is due to step S1.3 and the availability of the TLE of the object.

Once the topocentric right ascension and declination profiles of the RSO are obtained, the OD process starts. The aim of the OD process is to estimate the state of the object at the epoch of the first measurement obtained during its passage in the FoV of the sensor. The process consists of a nonlinear least square optimization to match the orbital trajectory with the range measurements, the Doppler shift measurements and the right ascension and declination time histories previously computed. The algorithm starts from an initial guess and propagates it in time using the high-fidelity propagator AIDA. The algorithm is the following:

- **OD 1.** Consider an initial guess for the RSO state vector at the epoch of the first measurement. In the case of known object, the guess is obtained by propagating the state vector provided by the TLE of the object till the first observation epoch by means of SGP4.

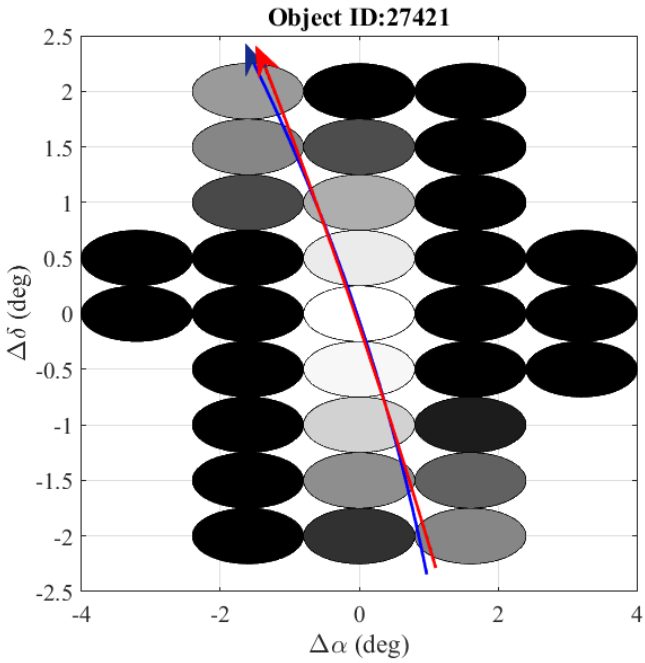

Figure 9. Right ascension and declination time history inside the receiver FoV for object 27421. The blue line is the result of S1, the red line corresponds to the refined $\alpha(t)$-$\delta(t)$ time histories (S2), whereas the black line (almost coincident with the red one) is the true trajectory

OD 2. Propagate the initial state and compute, for each observation instant, the state vector of the observed object, deriving the values of slant range, Doppler shift, topocentric right ascension and declination.

OD 3. Evaluate the residuals of the four quantities with respect to the measured values.

OD 4. Update the initial guess.

The algorithm provides the estimated state vector at the epoch of the first observation and the related covariance matrix.

4.2 Unknown Objects

The case of unknown object refers to OD process performed for an object whose TLE is not available to the user. The algorithm described in the previous section is slightly modified in this case. The unavailability of the TLE does not allow to exploit the knowledge of the state vector for both the estimation of the topocentric right ascension and declination profiles of the object, and the generation of the first guess for the orbit determination process. The first issue is solved by reducing the S1 procedure to its first two steps (S1-1 and S1-2): essentially, the first guess for $\Delta\alpha(t)$ and $\Delta\delta(t)$ is generated considering only the available SNR measurements. Moreover, during the S2 procedure, the radar cross section of the object is included in the set of unknowns of the least square fit. For the second issue, the first guess for the orbit determination process is generated (GG) assuming a motion on a circular orbit. The algorithm is the following:

GG 1. Sort the beams of the receiver according to their maximum measured SNR during the observation window.

GG 2. Identify the beam with maximum illumination during the passage of the object and the corresponding observation epoch t_1.

GG 3. Assume that the object passes at the centre of the beam at t_1, consider the line of sight of that beam and identify on it the point of minimum distance between this direction and the line of sight of the transmitter at epoch t_1. Define the related position vector $\boldsymbol{r}_1$. Under the presented assumptions, $\boldsymbol{r}_1$ represents the position vector of the observed object at epoch t_1.

GG 4. Assuming a circular motion, consider the second beam of the list and identify the position vector $\boldsymbol{r}_2$ at epoch t_2 as the one intersecting the beam line of sight with modulus $||r_1||$.

GG 5. Evaluate the orbital parameters of the circular orbit starting from $\boldsymbol{r}_1$ and $\boldsymbol{r}_2$.

GG 6. Compute the position and velocity vectors of the RSO at the first observation epoch.

The accuracy in the determination of the first guess is strictly related to the validity of the approximations made in the process. In particular, the accuracy of the two position vectors $\boldsymbol{r}_1$and $\boldsymbol{r}_2$ drastically decreases as the actual position of the object at t_1 and t_2 moves away from the centre of the selected beams, and this is likely to occur when the maximum detected SNR of those beams is low.

This is the reason why the two beams with the largest measured SNR are selected. The same approach is used for highly-elliptical orbits despite the assumption of circular orbit loses its validity.

Once the first guess is defined, the OD process is performed by relying on simple two-body dynamics due to the unavailability of the ballistic coefficient of the object.

5 NUMERICAL SIMULATIONS

The results of the performed numerical simulations are presented in this section. An observation window of two days is assumed, covering the range May 25-26, 2016. The main characteristics of the transmitter and the receiver in the analysed configuration are presented in Tab.1.

Table 1. Transmitter and Receiver characteristics

	Latitude	Longitude	Alt.	Diam.	Power
TX	39°45'31''N	9°27'01''E	205m	7m	10 kW
RX	44°31'25''N	11°38'59''E	25m	-	-

The beam configuration of the receiver is the one shown in Fig. 8, with 32 beams in symmetric configuration.

The analysis covers both the cases of known and unknown objects, studying the impact of measurement noise on the accuracy of the orbit determination results.

5.1 Known Objects

The case of known object with no noise measurements represents the first test for the tool. Measurement noise represents the deviation between the reality and the mathematical model used to describe it.

The number of catalogued objects is 5100, and only 283 can be observed (i.e., have a passage in the FoV of the sensor and generate a detectable SNR level). The reference condition for the error computation is evaluated by propagating the state vector provided by the TLE using AIDA up to the epoch of the first measurement. Tab.2 shows the results of the accuracy in position in terms of 50th and 75th percentile of the position error in radial direction ($\varepsilon_{p,rad}{}^{50\%}$ and $\varepsilon_{p,rad}{}^{75\%}$), 50th percentile of the position error ($\varepsilon_p{}^{50\%}$) and 50th percentile of the standard deviation in position ($\sigma_p{}^{50\%}$). As can be seen, all errors in positions are below 1m. Moreover, the analysis shows that all objects have a position error in radial direction lower than 100m.

Table 2. Accuracy in position for the case of known object with no measurement noise

$\varepsilon_{p,rad}{}^{50\%}$	$\varepsilon_{p,rad}{}^{75\%}$	$\varepsilon_p{}^{50\%}$	$\sigma_p{}^{50\%}$
0.176m	0.506m	0.91m	0.56m

This trend is quite expected, as the investigated case is the simplest possible, i.e. no disturbances introduced by measurement noise.

The performances of the simulator in terms of accuracy in velocity for all the objects with radial error in position lower than 100m are shown in Tab.3. The selected parameters are:

- 50th percentile of the error in transversal velocity $\varepsilon_{v,tr}{}^{50\%}\big|_{\varepsilon_{p,rad<100m}}$,
- 75th percentile of the error in transversal velocity $\varepsilon_{v,tr}{}^{75\%}\big|_{\varepsilon_{p,rad<100m}}$,
- 50th percentile of the standard deviation in velocity $\sigma_v{}^{50\%}\big|_{\varepsilon_{p,rad<100m}}$.

Table 3. Accuracy in velocity for the case of known objects with no measurement noise

$\varepsilon_{v,tr}{}^{50\%}\big\|_{\varepsilon_{p,rad<100m}}$	$\varepsilon_{v,tr}{}^{75\%}\big\|_{\varepsilon_{p,rad<100m}}$	$\sigma_v{}^{50\%}\big\|_{\varepsilon_{p,rad<100m}}$
0.015m/s	0.042m/s	0.04m/s

As expected, all terms are very low, and far below 1m/s.

It is now interesting to study the performance of the tool in case of presence of measurement noise. The first analysis is done assuming a noise on the slant range (SR) and Doppler shift (DS) measurements. The noise in the slant range is modelled assuming a Gaussian distribution with zero mean and a standard deviation of 3m. The Doppler shift noise is modelled by assuming a resolution of 20 Hz.

The results for the case under study are shown in Tab.4, second line. As can be seen, the accuracy is worse than in the previous case, though still all objects show a radial error in position lower than 100m. In particular, position errors increase of one order of magnitude, whereas the decrease in accuracy for the velocity components is more significant.

Overall, the influence of the introduced measurement noise is evident, though acceptable.

Table 4. Performances of the sensor for the case of known object, standard beam configuration

	n_{obj}	${\varepsilon_{p,rad}}^{50\%}$	${\varepsilon_{p,rad}}^{75\%}$	${\varepsilon_{p}}^{50\%}$	${\sigma_{p}}^{50\%}$	${\varepsilon_{v,tr}}^{50\%}\big\vert_{\varepsilon_{p,rad}<100m}$	${\varepsilon_{v,tr}}^{75\%}\big\vert_{\varepsilon_{p,rad}<100m}$	${\sigma_{v}}^{50\%}\big\vert_{\varepsilon_{p,rad}<100m}$
No noise	283	0.176m	0.506m	0.91m	0.56m	0.015m/s	0.042m/s	0.04m/s
Noise in SR and DS	278	1.62m	3.48m	6.96m	101.6m	1.4m/s	3.05m/s	6.6m/s
Noise in SR, DS and SNR	275	44.5m	76.4m	245m	130m	3.19m/s	5.7m/s	7.8m/s

The measurement noise is finally added to the SNR profiles as a white Gaussian noise, assuming a ratio of 30 dB between the nominal signal and the added white noise. The results of a simulation including all the three contributions to the measurement noise are shown in the third line of Tab.4. As can be seen, the combination of all three measurement noises causes a relevant decrease in the accuracy of the results in both position and velocity. However, the algorithm can identify more than 80% of the objects with a radial error in position lower than 100m.

5.2 Unknown Objects

The performance of the sensor in case of unknown objects is now investigated. The inaccuracy in the pointing of the receiver due to the unavailability of the TLE of the object is here modelled as a random error of ±2.5° in the elevation of the receiver with respect to the pointing computed by the simulator.

The results of unknown object and no measurement noise are shown in Tab.5, first line. A comparison with the analogous case of known object shows how the error significantly increases when the object is not known a priori. This can be explained with the fact that the unavailability of the TLE in some cases prevents the algorithm from precisely identifying the right ascension and declination profiles of the object, leading to a partially or totally wrong orbit determination. However, the algorithm is still able to perform the orbit determination granting a radial error in position below 100m for more than the 80% of the cases.

If measurement noise is considered, the results shown in the second and third lines are obtained. While the introduction of measurement noise on slant range and Doppler shift has a stronger effect on the accuracy in velocity, the combination of all three contributions drastically increases all the errors. The comparison between the two extreme cases of the presented simulations (known objects without measurement noise and unknown objects with all measurement noises) clearly shows how the performance of the algorithm strongly depends on the availability of the TLE of the object and the noise level. Overall, the last case represents, as expected, the most critical situation.

Fig.10 shows the trend of the cumulative error in transversal velocity for all the objects with $\varepsilon_{p,rad}$ lower than 100m. It is interesting to study the trend of the cumulative error in the most critical case (red line). As can be seen, while almost 80% objects show an error in transversal velocity lower than 10m/s, few objects have an error much larger than 100m/s, resulting to an average error of 106.8m/s.

5.3 Alternative beam configurations

The analysis presented in the previous section has shown how the case of unknown object represents the most critical one, with a significant decrease in accuracy in case of measurement noise. As the configuration of the pattern of beams of the receiver represents the main available degree of freedom, it is now interesting to study the performances of the sensor with different beam configurations. In this section, two alternative beam configurations are presented, and the analysis is done for the case of unknown objects with noise in all measurements.

Table 5. Performances of the sensor for the case of unknown object, standard beam configuration

	n_{obj}	${\varepsilon_{p,rad}}^{50\%}$	${\varepsilon_{p,rad}}^{75\%}$	${\varepsilon_{p}}^{50\%}$	${\sigma_{p}}^{50\%}$	${\varepsilon_{v,tr}}^{50\%}\big\vert_{\varepsilon_{p,rad}<100m}$	${\varepsilon_{v,tr}}^{75\%}\big\vert_{\varepsilon_{p,rad}<100m}$	${\sigma_{v}}^{50\%}\big\vert_{\varepsilon_{p,rad}<100m}$
No noise	276	0.64m	8.9m	4.18m	1.2m	0.032m/s	0.1m/s	0.061m/s
Noise in SR and DS	277	2.66m	16.2m	13.3m	111m	1.68m/s	3.76m/s	6.7m/s
Noise in SR, DS and SNR	257	96.3m	257.3m	509.1m	147.6m	4.4m/s	9.05m/s	8.05m/s

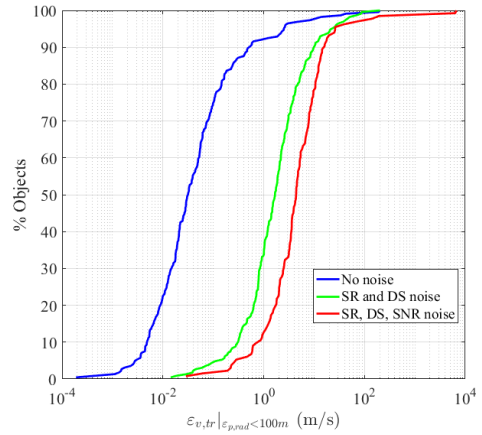

Figure 10. Cumulative error in transversal velocity for all objects with $\varepsilon_{p,rad}$ lower than 100m (unknown object, standard configuration)

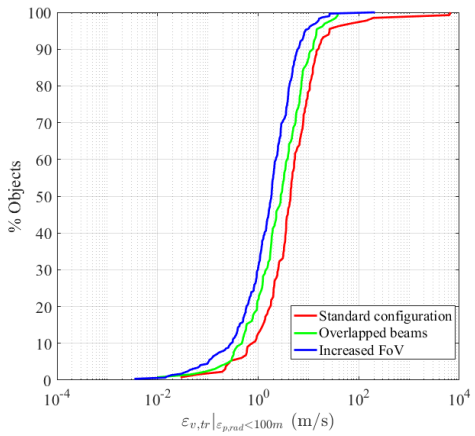

Figure 11. Cumulative error in transversal velocity for objects with $\varepsilon_{p,rad}$ lower than 100m (unknown object, noise in SR, DS, SNR)

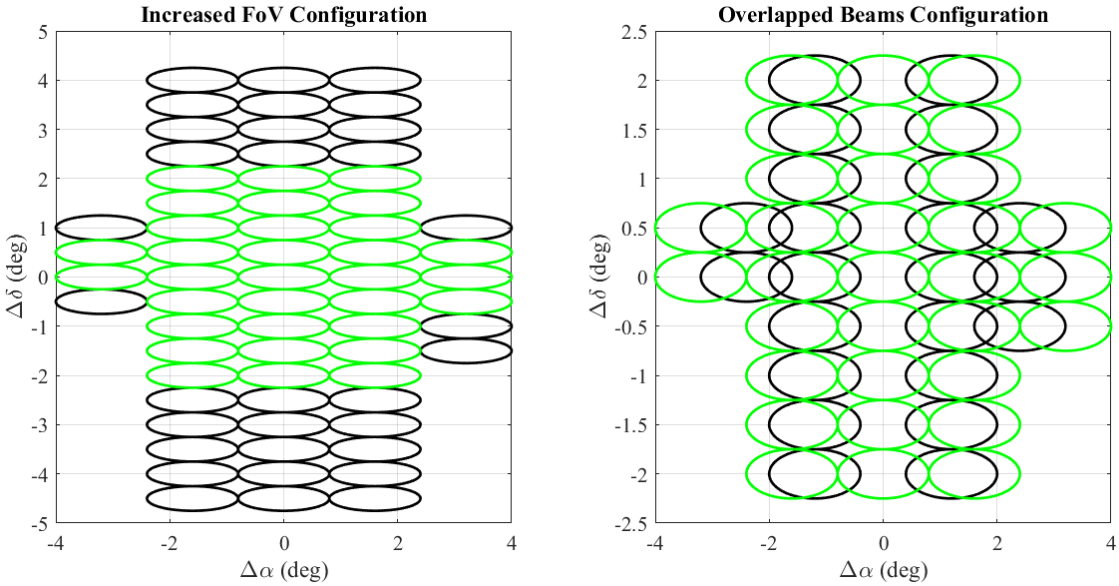

Figure 12. In black: increased FoV configuration (left) and overlapped beam configuration (right). In green: standard beam configuration.

Table 6. Comparison of the performances of the algorithm with different beam configurations of the receiver (case of unknown objects, measurement noise in SR, DS and SNR)

	n_{obj}	${\varepsilon_{p,rad}}^{50\%}$	${\varepsilon_{p,rad}}^{75\%}$	${\varepsilon_{p}}^{50\%}$	${\sigma_{p}}^{50\%}$	${\varepsilon_{v,tr}}^{50\%}\big\vert_{\varepsilon_{p,rad}<100m}$	${\varepsilon_{v,tr}}^{75\%}\big\vert_{\varepsilon_{p,rad}<100m}$	${\sigma_{v}}^{50\%}\big\vert_{\varepsilon_{p,rad}<100m}$
Standard configuration	257	96.3m	257.3m	509.1m	147.6m	4.4m/s	9.05m/s	8.05m/s
Overlapped beams	208	63.4m	136.5m	353.1m	130.9m	2.8m/s	6.6m/s	7.78m/s
Increased FoV	416	53.5m	119.2m	289.4m	92.3m	1.8m/s	3.79m/s	3.66m/s

The first beam configuration is presented in Fig.12 (right): the centers of the 32 beams are slightly shifted to obtain beam overlapping. The second beam configuration is shown on the left in the same figure: the number of beams is doubled with respect to the nominal configuration, so that the overall field of view of the sensor is increased. A comparison of the performance of the sensor in the standard configuration with these two alternative configurations is presented in Tab.6. As can be seen, both configurations allow to increase the accuracy of the orbit determination process both in position and velocity. In particular, the increased-FoV configuration represents the best option, allowing a significant reduction of all the considered figures of merit.

Fig.11 shows the same plot of Fig.10 for the three analysed configurations: again, it is evident how both alternative configurations guarantee a general improvement of the accuracy in velocity.

Finally, it is worth comparing the accuracy of the results by focusing on the objects of the catalogue that are observed in all three cases. Fig.13 shows the error in radial position for the standard configuration and the one with overlapped beams. As the trends show, the accuracy granted by the overlapped beams is almost always higher, apart from those cases for which the error granted by the standard configuration is already very low. In general, the advantages in exploiting the new configurations become more evident as the error in position increases.

The same analysis has been performed for the configuration with increased field of view, as shown in Fig.14. All the considerations made on the previous comparison hold.

6 CONCLUSIONS

The performance of the BIRALES radar sensor in terms of the achievable accuracy of the orbital estimation process on a catalogue of resident space objects has been assessed through numerical simulations. A simulator was developed to produce observation data in terms of SNR, Doppler shift, and time delay profiles during the passage in the volume defined by the intersection of the transmitter and receiver beams. The simulator allowed to test different beamforming geometries for the receiver, using different locations for each beam. The simulations show that the sensor, provided with its tailored OD algorithm, can estimate the orbital states with reasonable accuracy with just a single pass for most objects in the catalogue. This preliminary analysis and results will be extended in future works. The simulated beams will be adapted to their final optimized configuration, the ranging will be modelled based on the performance of the final transmitter, and the simulator and the OD algorithm will be calibrated using data from real observation campaigns. In addition, different beamforming geometry will be tested to support the possible upgrade strategies for the Northern Cross, taking into account the complete refurbishment of the antenna. The large area of approximately 31,000 m^2 could provide a high sensitivity and the maximum FOV of 120 deg^2 could be plastered with up to 46,000 beams 4'x4' wide.

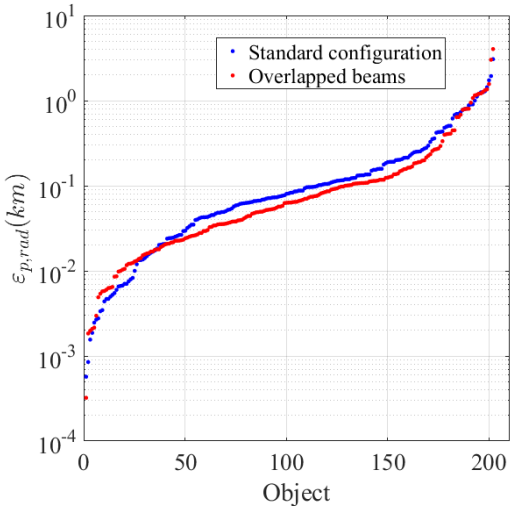

Figure 13. Position error in radial direction for standard and overlapped beams configuration

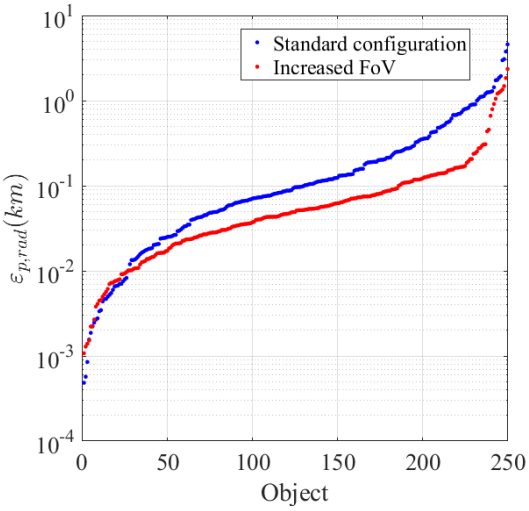

Figure 14. Position error in radial direction for standard and increased-FoV configuration

Acknowledgment

The authors acknowledge the support of the Italian Space Agency and the Italian National Institute of Astrophysics through the grant agreement n. 2015-028-R.O. (Space Debris – IADC activities support and SST pre-operative validation). The Flight Termination System is a facility of the Italian Air Force, located at Italian Joint Test Range of Salto di Quirra in Sardinia. The Northern Cross radiotelescope is a facility of the University of Bologna operated under agreement by the Radio Astronomy Institute of the Italian National Institute of Astrophysics.

7 REFERENCES

1. T. Flohrer, H. Krag, S. Lemmens, B. Bastida Virgili, K. Merz, and H. Klinkrad, Statistical Look on ESA's Conjunction Event Predictions, Proc. of the 6th Europ. Conf. on Space Debris, Darmstadt, Germany, ESA, SP-723, 2013.
2. C. Pardini, L. Anselmo, Re-entry predictions of three massive uncontrolled spacecraft, in 23rd International Symposium on Space Flight Dynamics, Pasadena, 2012.
3. Decision N. 541/2014/EU of the European Parliament and of the council, 16 April 2014.
4. http://www.esa.int/Our_Activities/Operations/Space_Situational_Awareness/About_SSA (accessed on March 29, 2017).
5. A. Morselli, P. Di Lizia, G. Bianchi, C. Bortolotti, S. Montebugnoli, G. Naldi, F. Perini, G. Pupillo, M. Roma, M. Schiaffino, A. Mattana, E. Salerno, A. Magro, K.Z. Adami, R. Armellin, A.L. Sergiusti, W. Villadei, F. Dolce, M. Reali, J. Paoli, A new high sensitivity radar sensor for space debris detection and accurate orbit determination, Metrology for Aerospace (MetroAeroSpace), 2015 IEEE.
6. S. Montebugnoli, G. Bianchi, J. Monari, G. Naldi, F. Perini, M. Schiaffino, "BEST: Basic Element for SKA Training". Wide Field Science and Technology for the Square Kilometre Array, Proc. Of the SKADS Conference held at the Château de Limelette, Belgium, 3-6 November 2009, p.331-336.